

pubs.acs.org/est Article

# Waste Combustion Releases Anthropogenic Nanomaterials in Indigenous Arctic Communities

Published as part of Environmental Science & Technology virtual special issue "Wildland Fires: Emissions, Chemistry, Contamination, Climate, and Human Health".

Julien Gigault,\* Caroline Guilmette, Huiwen Cai, Charlotte Carrier-Belleau, Marie Le Bagousse, Adèle Luthi-Maire, Manon Gibaud, Armelle Decaulne, Mahbub Alam, and Mohammed Baalousha\*

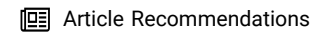


Cite This: Environ. Sci. Technol. 2024, 58, 15170–15180



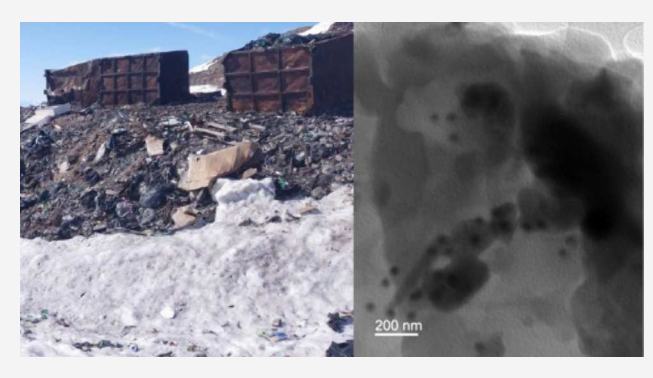
**ACCESS** 

III Metrics & More



s Supporting Information

ABSTRACT: Arctic autochthonous communities and the environment face unprecedented challenges due to climate change and anthropogenic activities. One less-explored aspect of these challenges is the release and distribution of anthropogenic nanomaterials in autochthonous communities. This study pioneers a comprehensive investigation into the nature and dispersion of anthropogenic nanomaterials within Arctic Autochthonous communities, originating from their traditional waste-burning practices. Employing advanced nanomaterials tools, we unraveled the nature and prevalence of nanomaterials, including metal oxides (TiO<sub>2</sub>, PbO), alloys (SnPb, SbPb, SnAg, SnCu, SnZn), chromated copper arsenate-related nanomaterials (CuCrO<sub>2</sub>, CuCr<sub>2</sub>O<sub>4</sub>), and nanoplastics (polystyrene and polypropylene) in snow and sediment near



waste burning sites. This groundbreaking study illuminates the unintended consequences of waste burning in remote Arctic areas, stressing the urgent need for interdisciplinary research, community engagement, and sustainable waste management. These measures are crucial to safeguard the fragile Arctic ecosystem and the health of autochthonous communities.

KEYWORDS: nanomaterials, waste, contaminant, incineration, Autochthonous community

#### INTRODUCTION

The Arctic region presents a unique challenge in solid waste management due to the presence of permafrost, which makes excavation extremely difficult. As a result, Northern Autochthonous communities employ distinct waste management practices compared to their subarctic counterparts. Whether in the Canadian Arctic, Greenland, or other arctic regions, the predominant approach to waste disposal involves open-air incineration of refuse, often without prior treatment. Notably, many of these incineration sites are located just a few hundred meters from residential dwellings, raising concerns regarding potential health and environmental impact. <sup>2,3</sup>

In the Nunavik region of Quebec, Canada, each individual generates approximately 27,000 kg of waste annually, resulting in a cumulative incineration of over 5000 tonnes<sup>4</sup> for the entire Nunavik region each year. Similarly, more than 10,000 tonnes of waste are incinerated in Greenland every year.<sup>5</sup> This waste includes household, residual materials from the municipal sector (including common plastics like polypropylene, polyethylene, and polystyrene), and electronic and construction material waste such as treated wood and paint. To deter wild

animals and reduce the perceived waste volume, communities practice open-air burning of this waste at least once a week.<sup>3</sup> It is well-known that open-air burning of waste generates ash and particulate matter with high levels of pollutants such as polycyclic aromatic hydrocarbon, dioxins, furans, polychlorobenzene, perfluoroalkyl substances, volatile organic compounds, metals and metalloids, and nanomaterials (NMs).<sup>6–9</sup> While the global dispersion and long-distance transport of contaminants within the Arctic ecosystem are well documented, there is a significant knowledge and data gap concerning the release and dispersion of locally generated contaminants such as those generated as a result of open-air waste burning practices. This knowledge gap assumes paramount importance as local sources of pollutants may

Received: March 19, 2024 Revised: July 29, 2024 Accepted: July 30, 2024 Published: August 14, 2024





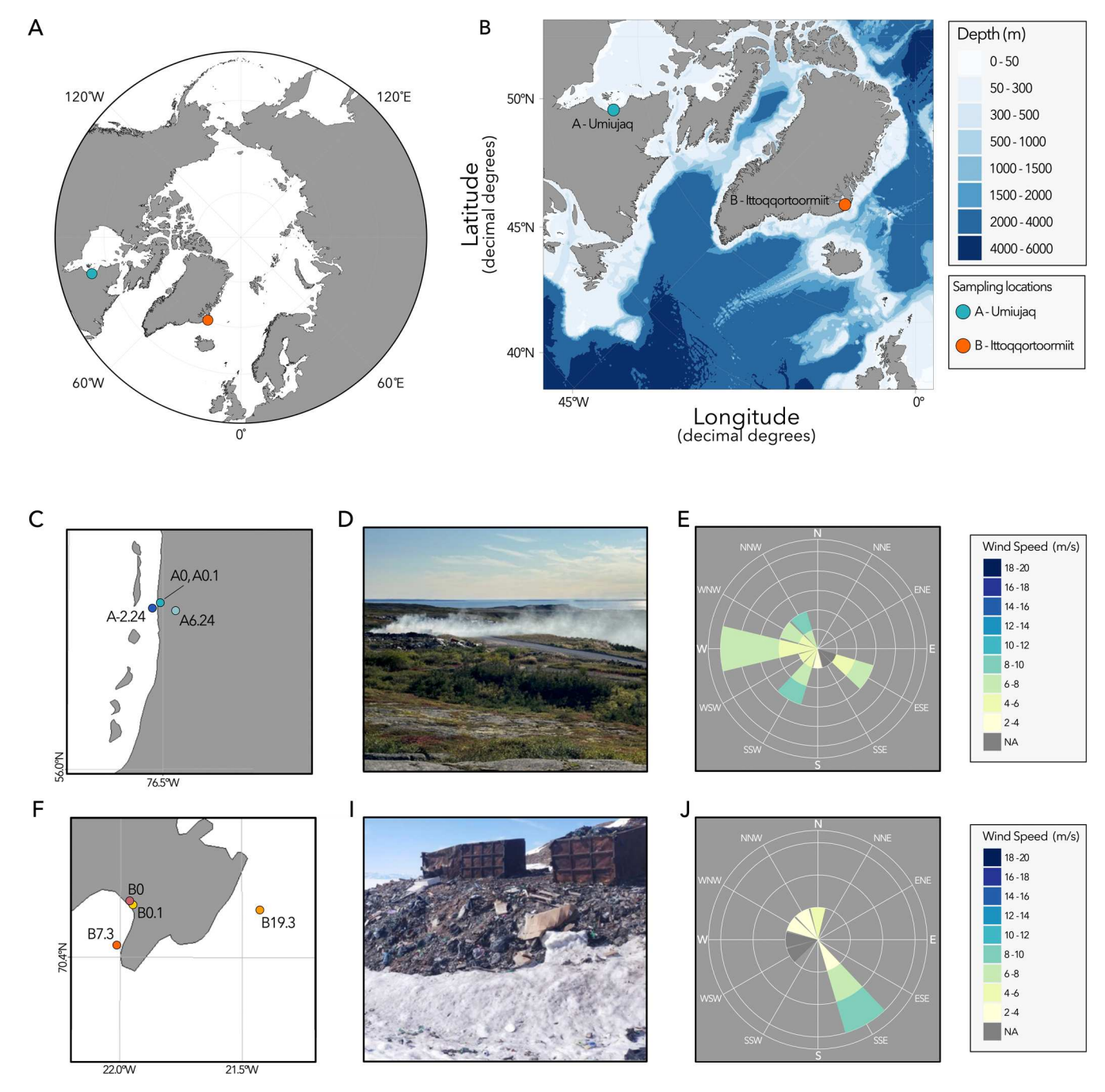


Figure 1. Maps of sampling locations indicating Inuit community villages in Canada and Greenland (A, B), waste dump sites (D, I), and sampling points (C and F). Pictures of three dumps, A: Umiujaq, Site A; B: Ittoqqortoormiit, Site B. At Site A, household waste composed of residual organic materials, electronic waste, and plastic materials, etc. are presorted and weekly burned due to local regulations. At Site B, waste is weekly burned without presorting. Panels C–J are sampling points upwind or downwind from the dumps. Panels E and J show dominant wind of the sampling sites during the past year. Specifically, E: August 1, 2022–July 31, 2022; J: May 30, 2022–June 5, 2022 (Permit G24-083 from Government of Greenland). Raw data of Site A was downloaded from Environment Canada-Hourly climate data (https://climate-change.canada.ca/climate-data/#/hourly-climate-data). Data of Site B is from World weather website (https://world-weather.info/archive/greenland/ittoqqortoormiit/#t2).

significantly exceed contributions from long-range transport pathways.

The overarching objective of this study is to investigate the nature, concentration, and dispersion of anthropogenic nanomaterials released from open-air waste-burning practices within Arctic communities. To this end, we collected snow and sediment samples at different locations upwind and downwind waste dump sites from two autochthonous communities

(Umiujaq, Site A, Canada; Ittoqqortoormiit, Site B, Greenland) employing different waste management practices. Samples labeling corresponds to their location relative to the prevailing wind direction and distance from the waste dump. Subsequently, we extracted nanomaterials from these samples and characterized their size distribution, composition, and concentration using state-of-the-art nanometrological approaches, including flow-field flow fractionation (AF4),

single-particle inductively coupled plasma time-of-flight-mass spectrometry (sp-icpTOFMS), pyrolysis-gas chromatography—mass spectrometry (py-GC-MS), and transmission electron microscopy (TEM).

#### **■ EXPERIMENTAL SECTION**

**Sampling Sites.** Solid-waste incineration emission impacted snow and sediment samples were collected from three northern communities in Greenland and Canada (Figure 1). The Canadian community is situated in Nunavik, on the Hudson Bay (Umiujaq, Site A, population of 541 in 2021). The second community is located on the East Coast of Greenland (Ittoqqortoormiit, Site B, population of 355 in 2019). For the two sites, waste is placed in a considerable container (up to 20,000 L) and burned at least once a week.

Sampling at Site A took place during the summer season. Sediments were collected as they were suspected of accumulating aerially transported nanomaterials. Notably, two sampling points at 2.1 km (A-2.1) and 2.4 km (A-2.4) upwind from Site A (on the beach) were shielded from the dominant winds. However, the beach could be contaminated with materials carried by the river that passes through the dump, which could be possibly contaminated by the exudate of the dump. A previous study used the same sampling protocol for sediment sampling. 10,11 At site B, 20 kg of snow samples were collected during the spring 2022 (Permit G24-083 from Government of Greenland), both upwind and downwind from the dump site. All of the samples collected on-site were directly stored in containers that had been previously checked and analyzed for potential contamination. As for the sediments, they were directly stored in an envelope and sealed, whereas the snow was collected in an airtight container and then dried under a laminar flow hood, followed by concentration through ultrafiltration in a mobile laboratory stationed on-site. Several experimental blanks were also studied using ultrapure water within the various sampling and sample storage systems. Lastly, we avoided working with polymers and metals that are likely to be present in the sampling materials. The samples were then sent to the laboratory for nanoparticle extraction

Nanoparticle Extraction from Environmental Matrices. Different extraction protocols were used for size and molecular characterization, according to the sample matrix. For the sediment samples from Site A, 20 g of sediment was mixed with 40 mL of KOH (0.5 mM) and agitated using an orbital stirrer for 24 h at 180 rpm (4G, machine information). The solution was centrifuged at 2000 rpm (500G,) for 10 min to separate the colloids from larger particles. The supernatant was isolated from the settled part using pipet.

For snow samples from Site B, 20 kg of snow were concentrated to 10 mL using a sequential Amicon ultra-filtration system equipped with a 150 kDa molecular weight cutoff (MWCO, poly(ether sulfone) NADIR membrane) and then freeze-dried. After that, 5 mg of freeze-dried particles was mixed in 1 mL of 0.5 mM KOH and shaken for 4 h at 180 rpm. The solution was centrifuged at 4000 rpm (1000G) for 10 min, and the nanoscale fraction (<1000 nm) supernatant was separated from the pellet. The use of a low ionic strength solution for nanoparticle dispersion does not impact the nanoparticle colloidal stability as demonstrated in previous studies using environmentally relevant model nanoplastics. Finally prior to PyGCMS analysis, nanomaterials were transferred into dichloromethane. To do so, for each sampling site, 1 mL of nanomaterials extracted from sediment (site A) or

snow (site B) were mixed with 1 mL of dichloromethane and sonicated in a bath for 30 min at 100 W. Then, the two phases were separated, and 80  $\mu$ L were deposited in the pyrolysis cup prior analysis.

Nanomaterial Size Characterization. Size characterization was conducted to ensure that only nanoscale matter was present in the solution before elemental and molecular characterization. Dynamic light scattering (DLS) and highresolution asymmetrical flow field fractionation (AF4) were employed for size characterization with UV and static light scattering spectrometry. A VascoFlex detector (Cordouan Technologies, France) equipped with a 633 nm red laser was used for DLS. Each measurement corresponds to 6 for 100 s. The AF4 instrument was a Postnova AF2000 coupled to a UV-visible spectrometer, a fluorescence spectrometer, and a multiangle light scattering detector (all from Postnova, Germany). The AF4 parameters and flow conditions were the same as Gigault et al. previously optimized. 13 Samples with the highest metal and nanoparticle concentrations (A0 and B0) also were characterized by transmission electron microscopy (TEM, JEOL JEM 2100 S/TEM, operated at 200 kV) to determine the morphology and elemental composition of NMs in the collected samples (see SI, section 1).

Molecular Characterization of Nanomaterials. A Pyrolyzer 3030D (Frontier Lab, Japan) coupled to a gas chromatography-mass spectrometry 5977B (Py-GCMS, Intuvo, Agilent Technologies) was used for molecular characterization of nanomaterials. Pyrolysis was performed at 600 °C for 30 s. The gas chromatography method is set as follows: 5 min at 50 °C, increasing to 180 °C at 5 °C/min, and to 310 °C at 10 °C/min and maintained for 20 min. Pyrolysis products were separated on a nonpolar gas chromatography column (DB5-MS, 60 m  $\times$  0.25 mm, 0.25  $\mu$ m film thickness, Agilent Technologies). The GCMS interface temperature was fixed at 300 °C. For the MS configuration: the ionization voltage was set at 70 eV, and an m/z range from 50 to 210 nm was analyzed with a 2000 Hz scanning frequency. For pyrolyzate identification, mass spectrum similarities to the NIST library spectrum were performed using the MSD ChemStation (Agilent Technologies). Procedure for polystyrene and polypropylene quantification is detailed in the Supporting Information (see SI, section S1)

**Total Metal Concentrations and Multielement Single** Particle Composition Analysis. For Site A samples, 100 mg of the sediment samples were digested using 1 mL of concentrated aqua regia ( $V_{HCl}$ :  $V_{HNO3}$  = 3:1) for 24 h. For Site B samples, 10 mg of the freeze-dried colloids were digested using 1 mL of concentrated aqua regia ( $V_{HCl}$ :  $V_{HNO3}$  = 4:1) for 24 h. After digestion, the digestates were diluted in 9 mL of ultrapure water (UPW, Millipore Advantage System, Merck Millipore, Darmstadt, Germany) and stored until analysis for total metal concentrations using inductively coupled plasma time-of-flight-mass spectrometry (ICP-TOF-MS). Prior to ICP-TOF-MS analysis, all samples were further diluted 10 to 50 times in 1% HNO<sub>3</sub>. Mass spectral calibration and routine tuning of ICP-TOF-MS were performed prior to analysis every day to achieve maximum sensitivity. Elemental concentration calibration was established using a series of ionic standards prepared in 1% HNO<sub>3</sub> from commercially available ICP multielement standards (BDH Chemicals, Radnor, PA, USA) with concentrations ranging from 0.001 to 100  $\mu$ g L<sup>-1</sup>.

The elemental particle composition at the individual particle level was determined by sp-icpTOFMS (TOFWERK, Thun,

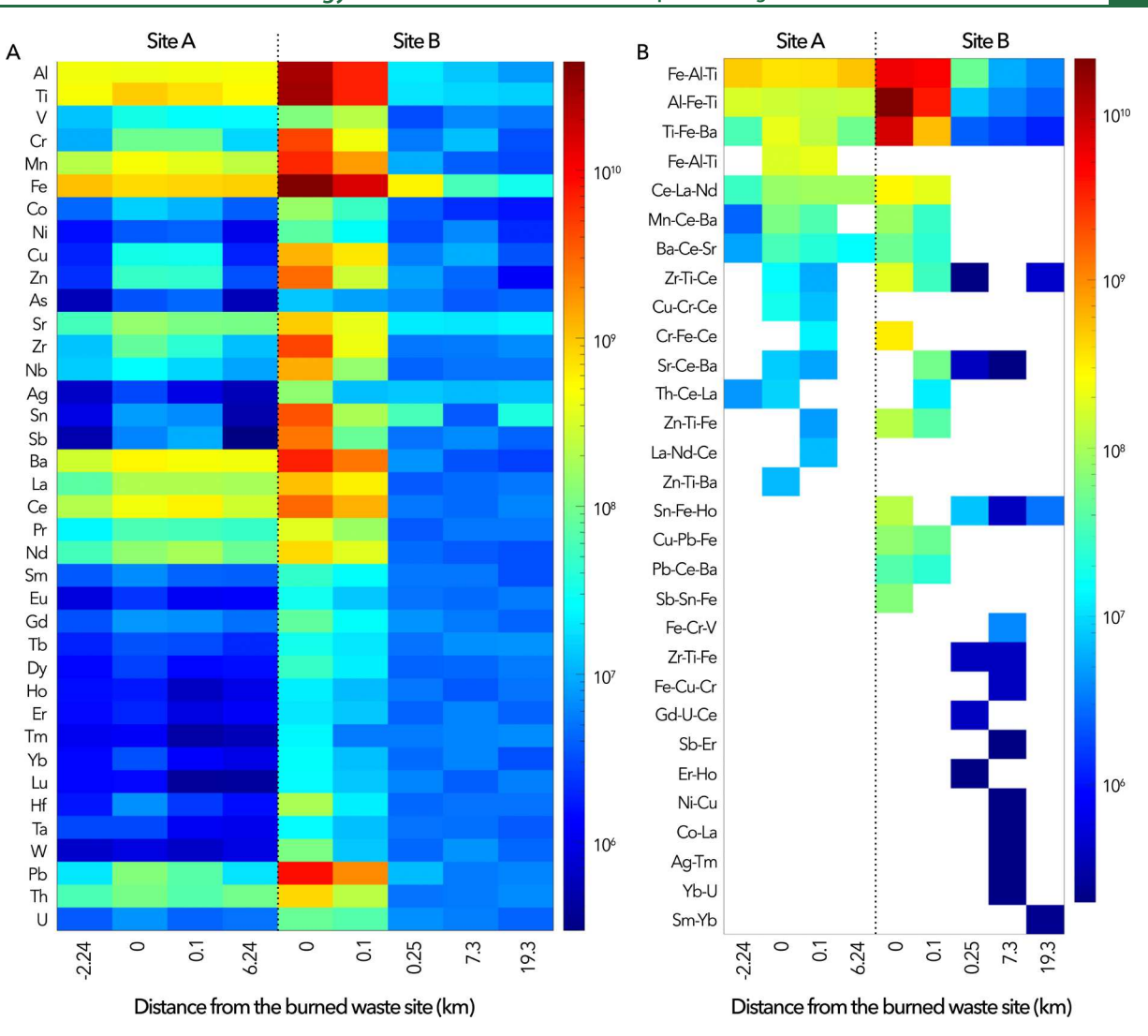


Figure 2. (a) Number concentration of nanomaterials in each sample from Site A (particle  $g^{-1}$  of sediment) and Site B (particle  $g^{-1}$  of freeze-dried colloids extracted from snow) as a function of distance from the burned waste dump. (b) The concentration (particle  $g^{-1}$ ) of multielement nanomaterials within each cluster identified in sediments at Site A and in snow at Site B as a function of distance from the burned waste dump. Negative distance indicates the upwind site, 0 indicates the dump site, and positive distance indicates downwind sites. Second stage cutoff = 0.154.

Switzerland) as described in our previous studies <sup>14,15</sup> and described in the Supporting Information (see section S1). The detected NMs were classified into single- and multimetals (smNMs and mmNMs). The mmNMs were further classified into clusters of mmNMs of similar elemental composition using two-stage (e.g., intra- and intersample) clustering analysis performed in MATLAB as described elsewhere. <sup>14</sup>

#### RESULTS AND DISCUSSION

Total Mass of Submicron Particles and Bulk Metal Concentrations and Ratios. Most metals and metalloids generally display higher concentrations at the Site B dump (B0) than at the Site A dump (A0). At Site B, the concentration of all elements, other than Sr and Ag, decreases with distance from the dump sites, indicating their release from waste incineration (see SI, Figure S2). Conversely, at Site A, elements of primary crustal origin, such as Al, Si, Fe, Zr, rare-earth elements, Th, and U, do not exhibit a discernible trend with distance from the waste dump site, as these elements naturally occur at elevated concentrations in sediments. In contrast, other elements such as Cr, Cu, Zn, As, Ag, Cd, Sn, Sb,

Ba, Pb, and Bi display an increasing trend from upwind to the dump site, followed by a decrease downwind with an increasing distance from the dump site, indicating their release from waste incineration.

Copper concentration reaches its highest level at the dump site and quickly diminishes to levels below the detection limit within a short distance from the dump site. In contrast, Zn, Pb, Ba, As, Cd, and Sb persist at concentrations above the detection limit even at greater distances (i.e., 10-20 km) from the dump site. The persistence of these elements indicates the long-distance transport of these elements, likely attributable to their higher volatility compared to Cu and their concurrent transport with the ash. 16,17 The distinct emission signal of these elements stems from their relatively low abundance in the earth's crust compared to elements, such as Al and Ti, which have higher background concentrations. Consequently, it is likely that other elements are released during waste combustion at the dump site; however, their signal might be dwarfed by the prevalent abundance of these elements in the Earth's crust.

At Site B, waste including vehicles, construction materials, and household garbage is burned without presorting, while at Site A, only presorted household waste is burned. This leads to a more diverse release of nanomaterials at Site B, often at higher concentrations compared to Site A. Additionally, the lower concentration of anthropogenic metal(loid)s at Site A, along with their high natural background concentrations in the sediment substrate, diminishes their signature compared to Site B. To distinguish between anthropogenic and natural sources of metal(loid)s, we analyzed elemental ratios such as Ti/Nb, Ce/La, Sn/Pb, and Sb/Pb. Ti/Nb and Ce/La ratios were selected as Ti and Nb as well as Ce and La naturally occur in association in several minerals and have been demonstrated to be an effective tool to differentiate natural from anthropogenic Ti and Ce. 18-21 The Sn/Pb and Sb/Pb ratios were selected because they occurred in many multielement particles detected by SP-ICP-TOF-MS as discussed below. Across all samples from Site B, these ratios exceed natural background levels, indicating an anthropogenic contribution of Ti, La, Ce, Sn, and Sb.

Single-Particle Analysis. Particle Number Concentration and Size Distribution. Consistent with the bulk metal concentrations (Figure S2) in the submicron particle fraction, the particle number concentration for all elements at B0 surpasses that at A0 by a substantial margin, ranging from 3- to 470-fold difference (Figure 2a). This divergence can be attributed to variations in sample matrices (sediments for Site A vs snow for Site B), the composition of the burned waste materials (household waste for Site A vs mixed construction, vehicle, and household waste for Site B), and the normalization (weight of sediment for Site A vs weight of extracted colloidal fraction for Site B).

For both sites, particle number concentration reaches its peak at the waste dump site, declining with distance from the dump site. Furthermore, at A0, the particle number concentration of all metal(loid)s, except for Al and Fe due to their naturally high background concentrations in sediments, is 2 to 21-fold higher than those observed at A-2.24, which is located upwind of the dump site. Elements commonly attributed to anthropogenic activities such as Zn, Cu, Sb, Cr, Sn, Zr, Pb, and As display the highest increases (>6 folds) from A-2.24 to A0. At site A, the number concentration decreases for all elements from the dump site (A0) to the nearest sampling location (A0.1), with the exception of As and Sb. This exception may be attributed to their volatilization due to their low boiling point and subsequent condensation downwind. These observations indicate contamination of sediment samples by NMs released from waste combustion.

At Site B, the concentration of all metalloids, except As, decreases to less than 5% of those at dump site B0 within distances ranging from 0.25 to 19.3 km. This observation indicates the long-distance transport of As compared to that of other metal(loid)s. The relatively high number concentrations (28 to 48%) of As-bearing NMs within distances of 0.25 to 19.3 km, relative to those at B0, align with the elevated total As concentration even at a distance from the dump site (Figure S2b). This occurrence is likely attributed to the volatilization and recondensation of As downwind, resulting in long-distance transport from the dump sites. <sup>16</sup>

Chromium, Cu, As, Sn, Sb, and Pb exhibit broader size distributions with higher median sizes at and near the burned waste dump sites (A0, A0.1, B0, and B0.1) compared to those upwind and downwind sites (Figure S4).

The rapid decrease of NM concentration and the decreases in NM size with distance from the dump site suggest the anthropogenic origin of the emitted NMs and their release from waste incineration practices at the waste dump sites.

Single-Particle Composition and Identification of Possible Nanomaterial Phases. Most (>50%) of the NMs in samples from Site A, B0, and B0.1, occurred as multimetal NM (mmNMs). We identified 30 clusters of mmNMs in both sediment and snow samples (Figure 2). The clusters Fe-Al-Ti, Al-Fe-Ti, Ti-Fe-Ba, Ce-La-Nd, and Mn-Ce-Ba constituted the majority of mmNMs, with concentrations ranging from 10<sup>8</sup> to 10<sup>10</sup> particles g<sup>-1</sup>. While some of these elemental combinations, such as Fe-Al-Ti, Al-Fe-Ti, Ti-Fe-Ba, and Ce-La-Nd, are typically detected in naturally occurring NMs, others such as Cu-Cr-Ce, Zn-Ti-Fe, Zn-Ti-Ba, Sn-Fe-Ho, Cu-Pb-Fe, and Sb-Sn-Fe are rarely detected at high frequency in natural NMs, indicating their anthropogenic origin. Elements such as Fe, Al, Ti, and Mn are abundant in the Earth's crust and are commonly found in natural NMs (Figure 2a). In contrast, V, Cr, Cu, Zn, As, Sn, Sb, Pb, and Ni are characteristic of anthropogenic metal(loid)s and are seldom detected in natural environmental samples. When detected, they typically occur at very low number concentrations. 14 These elements have been detected in nanoplastics and urban runoff, 15,22 wildland-urban interface fire ashes,<sup>23</sup> and ashes from chromated copper arsenate treated wood.<sup>24</sup> Similarly, mirroring the total particle number concentration, the highest concentrations of mmNMs were observed in samples collected at the dump sites (A0 and B0) and decreased with distance from these sites (Figure 2b), indicating the anthropogenic nature of these mmNM clusters and their origin from the dump site. In the following sections, we discuss specific clusters and elemental ratios to further illustrate the anthropogenic nature of certain classes of NMs.

Aluminum- and Titanium-Bearing NMs. Clusters rich in Al and Ti within the mmNM exhibit significant variation in the Fe mass fractions within this cluster (Figure S6). Al/Fe and Ti/Fe ratios show significantly higher values in samples from Site B (Figure S7b,d) compared to those from Site A (Figure S7a and c). Given that Site A samples consist of sediments, it is likely that natural NMs predominantly contribute to the extracted nanomaterials, thereby resulting in a relatively smaller anthropogenic signature at Site A. For instance, lower Ti/Fe ratios (ranging between 0.1 and 0.2) are more prevalent for all sampling points within Site A. In natural minerals, Ti and Fe occur in various forms: titanomagnetite  $(Fe_{3-x}Ti_xO_4, 0 < Ti/Fe < 0.43, 0 < x < 1)$  which form a complete solid solution series between end members of magnetite (Fe<sub>3</sub>O<sub>4</sub>, Ti/Fe = 0); ulvöspinel (Fe<sub>2</sub>TiO<sub>4</sub>, Ti/Fe = 0.43); pseudobrookite (Fe<sub>2</sub>TiO<sub>5</sub>, Ti/Fe = 0.43); and ilmenite (FeTiO<sub>3</sub>, Ti/Fe = 0.86). The Ti/Fe ratios in the NMs at Site A suggest a natural origin. Conversely, Site B samples are composed of snow samples and are likely dominated by an anthropogenic signature, albeit with a minor contribution from natural sources. Nanomaterials exhibiting high Al/Fe (ranging from 2.0 to 100) and Ti/Fe (ranging from 2.0 to 1000) at both sites A and B can be attributed to heteroaggregation of anthropogenic pure Al- and Ti-NMs (e.g., Al<sub>2</sub>O<sub>3</sub> and TiO<sub>2</sub>) with natural Fe-bearing NMs. It is plausible that the pure Al and Ti-bearing NMs originate from sources such as paints or plastics.<sup>25</sup>

Cerium- and Lanthanum-Bearing Particles. Nanomaterials containing cerium (Ce) and lanthanum (La) exhibit a

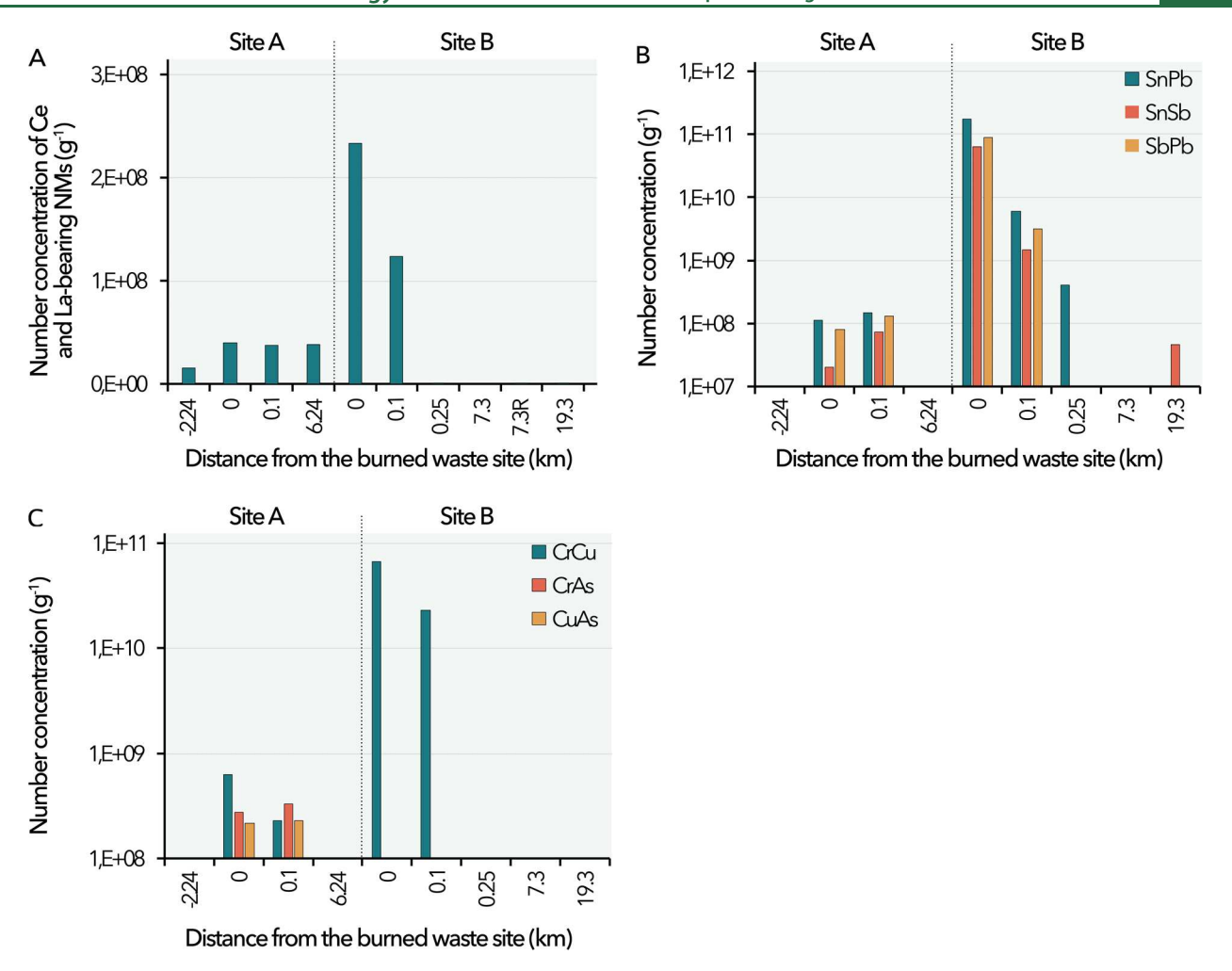


Figure 3. Number concentration of select classes of anthropogenic nanomaterials identified in sediments (site A) and snow (site B) as a function of the distance (kilometers) from the burned waste dump site: (a) Ce- and La-bearing NMs, (b) SnPb-, SnSb-, and SbPb-bearing nanomaterials, and (c) CrCu-, CrAs-, and CuAs-bearing nanomaterials. Negative distance indicates upwind site, 0 indicates the dump site, and positive distance indicates downwind sites.

wide-ranging distribution of Ce/La ratios, akin to those found in naturally occurring Ce-La-bearing NMs or incidental Ce-La NMs. A substantial fraction of NMs at A0.1 and B0 sites exhibits high Ce/La ratio (Figure S8), extending up to Ce/La exceeding 500. Prior investigations have shown that incidental Ce-La-bearing NMs have similar elemental ratios to natural Ce-La-bearing NMs. The probability of Ce-La particles with a high Ce/La ratio is higher at the dump site and decreases with distance from the dump site to downwind points.

The number concentration of Ce-La-bearing NMs increases from the upwind to the dump site at Site A and site B. At Site A, the number concentration of Ce-La-bearing NMs remains constant with the distance from the dump site, likely due to the dominance of natural Ce-La-bearing NMs in the sediments (Figure 3a). In contrast, at Site B, the number concentration of Ce-La-bearing NMs decreases with distance from the dump site, eventually disappearing entirely at a distance of 0.25 km downwind. This observation suggests the anthropogenic nature of Ce-La NMs emitted from solid waste combustion.

**Chromium-Bearing Particles.** A wide and substantial portion (ranging from 11% to 70%) of Cr-bearing NMs was found to be associated with Fe-bearing NMs. To elucidate

their origin, we analyzed the elemental ratios of Cr/Fe (Figure S9). These Cr/Fe ratios exceeded the average crustal ratio of 0.00235 in both Site A and Site B, with Site B displaying higher values compared to Site A (Figure S9). This pattern underscores the anthropogenic nature of these particles. Clustering analysis, focusing on chromium-rich particles after removing Al, Ti, Mn, and Fe revealed 14 clusters. Among the 14 clusters, one was identified as Cr-rich, while the remaining 13 clusters contained Cr as the second or third most abundant element (Figure S10). These Cr clusters are associated with metal chromate particles such as copper chromate (CuCrO<sub>2</sub>, CuCr<sub>2</sub>O<sub>4</sub>, Figure S10e), barium chromate (BaCrO<sub>4</sub>, Figure S10f), zinc chromate (ZnCrO<sub>4</sub>, Figure S10g), vanadium chromate (V<sub>2</sub>(CrO<sub>4</sub>)<sub>5</sub>, Figure S10h), zirconium chromate (ZrCrO<sub>4</sub>, Figure S10j), tin chromate (Sn(CrO<sub>4</sub>)<sub>2</sub>, Figure S10k), arsenic chromate (CrAsO<sub>4</sub> and CrAs<sub>2</sub>O<sub>6</sub>, Figure S10l), antimony chromate (SbCrO<sub>4</sub>, Figure S10m), strontium chromate (SrCrO, Figure S10n), lead (di)chromate (PbCrO<sub>4</sub> or PbCr<sub>2</sub>O<sub>7</sub>, Figure S100 and q), and nickel chromate (NiCrO<sub>4</sub>, Figure S10p).

The high number concentrations of Cr, Cu, and As, along with the presence of two clusters associating these three elements (Cu-Cr-Ba and As-Cr-Cu, Figure S10e and l), suggest that these elements may originate from the combustion

of chromated copper arsenate (CCA) treated wood. At A0 and A0.1, the majority of As-bearing NMs were associated with Cr (78-80%) and Cu (54-63%) with a mean mass fraction (Cr<sub>0.51</sub>Cu<sub>0.25</sub>As<sub>0.22</sub>). Similarly, most Cu was associated with Cr (52%). In contrast, none of the As-bearing NMs at sites A-2.2, A6.24 were associated with Cr or Cu. Similarly, the majority of As occurred as smNM Site B samples. The molar elemental ratios of Cr/Cu, Cu/As, and Cr/As are typical of those detected in ash from chromated copper arsenate treated wood (Figure S11), indicating that these two clusters of Cr-, Cu-, and As-bearing NMs can be attributed to the presence of chromated copper arsenate (CCA) particles, primarily used in construction materials.<sup>24</sup> The molar element ratio of Cr/Cu exhibits a broad distribution between 0 and 5, with median ratios of 1.0-2.0. These ratios can be attributed to CuCrO<sub>2</sub> and CuCr2O4, whereas higher ratios can be ascribed to aggregates of these phases with Cr single-metal NMs (smNMs). The Cr/As and Cu/As molar ratios for Sites A0 and A0.1 exhibit broad distributions between 0.5 and 10 and 0.5 and 5, respectively. The Cr/As ratios of 0.5 and 1 can be ascribed to phases such as CrAs<sub>2</sub>O<sub>6</sub> and CrAsO<sub>4</sub>. The higher ratios can be attributed to the aggregation of smNMs and mmNMs that contain Cr, Cu, and As, and the volatilization of As during the combustion of CCA-treated wood. The number concentration of Cu-Cr-Ba mmNMs is higher at A0 and B0 than at A0.1 and B0.1, respectively (Figure S10a). The number concentration of As-Cr-Cu mmNMs is higher at A0.1 than at A0, likely due to the vaporization of As during waste combustion and recondensation with cooling downwind.<sup>27</sup> Chromated copper arsenate has been widely used as a wood treatment to protect wood products and timber from insects, pests, and microbes.<sup>2</sup>

The mass elemental ratios of Ba/Cr, Sr/Cr, and Zr/Cr are generally lower than the average crustal ratios (Figure S12ac). They align with ratios found in specific compounds such as BaCrO4, SrCrO, and ZrCrO4, but also vary due to the presence of multiple chromate phases and heteroaggregation. Pb/Cr, Zn/Cr, and V/Cr ratios show broad distributions, with some values exceeding typical cluster ratios, possibly due to the presence of pure metal particles in aggregates with other phases (Figure S12d-f). Sn/Cr and Sb/Cr ratios are higher than average crustal ratios and align with the ratios found in SnCrO<sub>4</sub> and SbCrO<sub>4</sub> (Figure S12g and h). These metalsbearing nanomaterials have various applications in plastics, serving as additives for pigments, fillers, stabilizers, catalysts, biocides, antimicrobial agents, lubricants, and flame retardants.<sup>29,30</sup> Commonly used fillers in plastics include SiO<sub>2</sub>, CaCO<sub>3</sub>, BaSO<sub>4</sub>, TiO<sub>2</sub>, clays, talc (MgSi<sub>4</sub>O<sub>10</sub>(OH)<sub>2</sub>), and kaolinite (Al<sub>2</sub>Si<sub>2</sub>O<sub>5</sub>(OH)).<sup>31</sup> Titanium in the form of TiO<sub>2</sub>, Zn in the form of ZnO and ZnS are used as white pigment; Cu in the form of BaCuSi<sub>2</sub>O<sub>6</sub>, and 2CuCO<sub>3</sub>·Cu(OH)<sub>2</sub> is used in the blue pigment; Cu, Cd, and Cr are used as green pigments such as the phthalocyanine green (Cu-organic complex), CuCH<sub>3</sub>COO)<sub>2</sub>·H<sub>2</sub>O, CuCO<sub>3</sub>·Cu(OH)<sub>2</sub>, Cr<sub>2</sub>O<sub>3</sub>·2H<sub>2</sub>O, and a mix of CdS and Cr2O3; Pb, Ba, and Sr are used as yellow pigments such as Pb<sub>3</sub>(SbO<sub>4</sub>)<sub>2</sub>, PbCrO<sub>4</sub>, and SrCrO<sub>4</sub> or Pb<sub>2</sub>SnO<sub>4</sub> and BaCrO<sub>4</sub>. Lead and Ba are also used in plastic formulations as heat stabilizers, antioxidants, UV stabilizers (Pb), and fillers (Ba). Antimony in Sb<sub>2</sub>O<sub>3</sub> and Zn is used in plastics as flame retardants. It can explain why these metal elements exist in the collected samples.

**Sn-, Sb-, and Pb-Bearing Nanomaterials.** Sn, Sb, and Pb are present as minor elements in clusters containing Al, Fe,

and Ti-rich particles. These elements aggregate with Al, Fe, and Ti in larger masses, prompting an assessment of their elemental ratios relative to associated elements at Site A and Site B. The mass elemental ratios of Sn/Fe, Sn/Al, and Sn/Ti exceed the crustal average, indicating their anthropogenic origin in these samples (Figure S13a-c). Conversely, Sn/Sb ratios are lower than average crustal values, which align with a series of SnSb<sub>3</sub>, SnSb<sub>2</sub>, SnSb, Sn<sub>3</sub>Sb, suggesting the presence of likely alloys or semiconductors with specific formulas (Figure S13d).<sup>32</sup> Overall, the findings underscore the anthropogenic influence on the presence and distribution of these elements in the analyzed samples. The elemental ratios of Sn/Pb are higher than the average crustal value (0.12, Figure S13e) and covers those of pigments such as  $Pb_2Sn_4$  (Sn/Pb = 0.29) and  $PbSnO_4$ (Pb/Sn = 0.57), or SnPb alloys such as PbSn<sub>3</sub> (Sn/Pb = 1.71) and  $PbSn_5$  (Sn/Pb = 2.86). The elemental ratios of Cu/Sn (Figure S13f), Zn/Sn, Ag/Sn, and Ce/Sn are consistent with those of Pb-free Sn alloys (Figure S13g-i and Table S3). 33,34 These elemental combinations and ratios could be attributed to SnSbPb-based and Pb-free alloys. Indeed, even if SnPb is the traditional solder alloy, other elements, such as Ag, Zn, Cu, In, Bi, and REE-doped Sn alloys, have been recently used to replace Pb.

Multimetal nanomaterials rich in antimony (Sb) are frequently found in association with iron (Fe), aluminum (Al), titanium (Ti), and lead (Pb). Elemental ratios of Sb/Al, Sn/Fe, and Sn/Ti exceed the crustal average ratio (Figure S14a, c), suggesting the anthropogenic nature of Sn. Moreover, the Sb/Pb ratio is higher than the average crustal value of 0.024 and coincides with a series of SbPb with the formula of SbPb<sub>y</sub> (y = 1 to >10), most likely alloys of SbPb, or semiconductors such as CuPbSbS<sub>3</sub>, Pb-Sb-Sn, Pb-Ag-Sb, and Pb-Sb-S (Figure S14d). 35,36

Nanoplastics. The submicron particles extracted from site A's sediments and site B's snow were characterized by pyrolysis-mass chromatography—mass spectroscopy (py-GCMS). The detected pyrolysates consist mainly of unsaturated aliphatic chains (alkenes and unSatH), aromatics (Ar), and some alcohols and ketones (AlOH, Figure S15). The low abundance of oxygenated pyrolyzates (such as phenol, cyclopentanone) compared to aliphatic and aromatics pyrolyzates (*n*-alkene, benzene, toluene, and styrene) suggest that the pyrolysates originate from oxygen-depleted material, such as soot or plastics and polymers. The pyrograms show a pronounced styrene peak, and less pronounced styrene dimer and 2,4-dimethyl-1-heptene (*m*/*z* 70 and 126, C9) peaks (Figures S15 and 16). These pyrolysates are well-known markers of polystyrene and polypropylene nanoplastics. 38

Styrene can be attributed to the pyrolysis of polystyrene nanoplastics and/or natural organic matter.  $^{38,39}$  The relative contribution of natural organic matter versus polystyrene can be estimated by determining the ratio of Toluene/Styrene (Tol/Sty) (Figure S17 and 18). A Tol/Sty ratio greater than 1 indicates that the samples are dominated by natural organic matter with a small contribution (20 to 40%) of polystyrene nanoplastics. In contrast, a Tol/Sty ratio less than 1 indicates that the polystyrene nanoplastics contribute at least 95% to the styrene signal.  $^{38,40}$  For A0, A0.1, and B0.1, the Tol/Sty ratio is <1, confirming that polystyrene nanoplastics is the main contributor (i.e., > 95%) to the styrene (m/z 104) signal, which can be used to quantify the concentration of polystyrene nanoplastics. For site B0, the Tol/Sty ratio exceeds 1, suggesting that organic matter contributes significantly to the

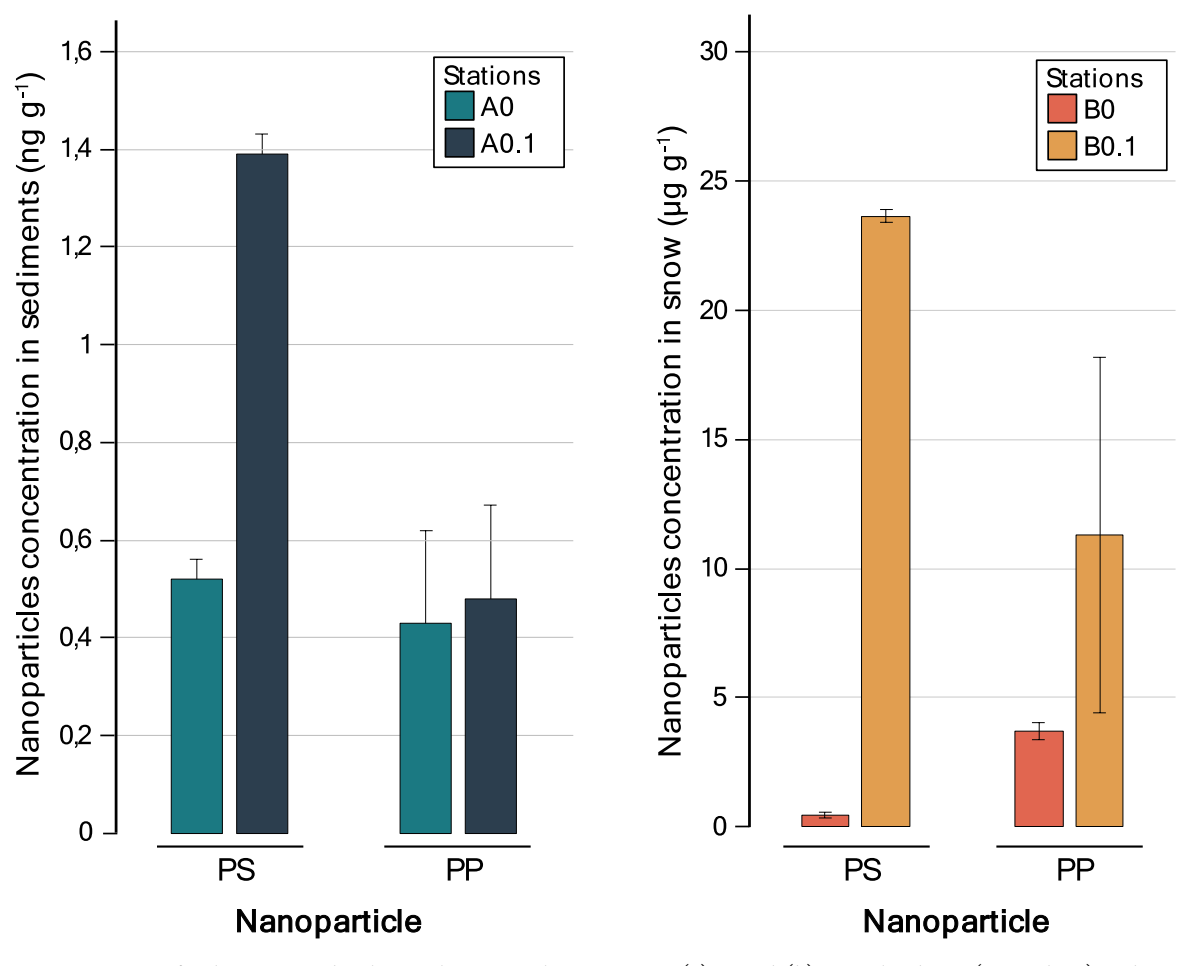


Figure 4. Concentration of polystyrene and polypropylene nanoplastics in sites (a) A and (b) B at the dump (A0 and B0) and up to 100 m downwind (A0.1 and B0.1). For the site A, concentrations are expressed in nanogram of nanomaterials per gram of sediment extracted from soil. For site B, concentrations are expressed in nanogram of nanomaterials per gram of particles extracted from the snow.

toluene signal, thereby influencing the Tol/Sty ratio such that polystyrene represents 20 to 40% of the styrene signal in comparison to natural organic matter. Furthermore, the presence of polystyrene nanoplastics in the studied samples was confirmed by tracking styrene dimer (m/z 91 at  $t_{\rm R}=24.6$  min) because the styrene dimer is a categorical indicator of polystyrene nanoplastics. Styrene dimer was detected in all samples, confirming that all samples contained polystyrene nanoplastics (Figure S16). However, the sensitivity to styrene dimer is notably lower than that of styrene (1% compared to the styrene) and varies with the size distribution of polystyrene particles, limiting the use of the styrene dimer peak to determine to determine the concentration of styrene nanoplastics. Thus, the concentration of polystyrene nanoplastics was determined using a styrene signal.

For site A0, we estimated the polystyrene nanoparticle concentration at 0.52  $\pm$  0.04 ng per g of sediment (Figure 4a). At a distance of 100 m from the landfill, the polystyrene concentration increases to 1.39  $\pm$  0.18 ng per g of sediment. For site B0, the concentrations of polystyrene nanoplastics are estimated to be 0.1  $\pm$  0.02 to 0.2  $\pm$  0.04  $\mu g$  g $^{-1}$  of particles extracted from the snow, assuming that polystyrene nanoplastics account for 20 to 40% of the styrene signal (Figure 4b). At B0.1 the concentration of polystyrene nanomaterials increases to 23.64  $\pm$  0.35  $\mu g$  g $^{-1}$ .

For polypropylene, several characteristic pyrolyzates have been attributed solely to this type of plastic without a contribution from natural organic matter, including 2,4-dimethyl-1-heptene (m/z 70 and 126, C9, Figure S17).<sup>39</sup> These pyrolyzates were identified in all sites with a higher relative abundance at 100 m (A0.1 and B0.1, Figure S18), a similar trend to polystyrene (Figure S19). At site A, the concentration of polypropylene increases from 0.43  $\pm$  0.02 to 0.48  $\pm$  0.12 ng per gr of sediment (Figure 4a). In the snow at both points, there is also a significant increase in polypropylene concentration from point B0 to point B0.1, going from 3.70  $\pm$  0.25 to 11.32  $\pm$  6.88  $\mu$ g of nanomaterials per gram of particles in the snow (Figure 4b). However, this increase is less pronounced than polystyrene, which could be attributed to the larger particle size of polystyrene compared to propylene or to the lower thermal decomposition stability of polystyrene compared to polypropylene.<sup>41</sup>

Similar to metals such as Cu, Ti, Sb, Sn, and Pb, nanoplastics show a similar trend: an increase from point 0 at the dump (A0 and B0) to 100 m. In fact, the concentration of Sb and Sb exhibit a good correlation with the concentrations of PS and PP (Figure S20). This association and correlation could be attributed to the use of Sb and Sn in production of plastics as heat stabilizers and flame retardants.<sup>25</sup>

The significant difference between sites A and B lies in the sampled matrix. In the case of site A, the sediments contain significantly more natural particles than the snow, which mainly contains combustion residues. Furthermore, cold spots are also known to concentrate contaminants, especially

nanomaterials.<sup>42</sup> The concentrations we measured align with the concentration the range of black carbon nanomaterials detected in Arctic ice cores, measured in nanograms per gram  $(ng\ g^{-1})$ .<sup>43</sup>

Nanomaterial Morphology and Chemical Composition. Analysis of the extracted submicrometer particles using TEM-EDS (Figure S20) shows several aggregates of nanomaterials in B0 with different morphologies and chemical composition, including spherical Ca-, Al-, Si-, and Fe-rich nanomaterials (Figure S21a), spherical Si- and Ti-rich nanomaterials (Figure S21b), needle-shaped Si- and Fe-rich nanomaterials (Figure S21c), and Mg-, Al-, Si-, Cl-, Ca-, Ti-, Fe-, and S-bearing nanomaterials (Figure S21d). Nanomaterials with similar morphologies and elemental composition were also observed in A0. It was possible to detect these nanomaterials as they are the dominant types of nanomaterials int the studied samples as determined by sp-icpTOFMS. However, it was not possible to detect other types (e.g., Cr, Cu, Sn, Sb, and Pb) of nanomaterials due to their low number concentrations compared to Al-, Si-, Ti-, and Fe-bearing nanomaterials, thus the very small probability (number of these NMs compared to the total number of detected particles <0.04) of finding such particles in the dominant background particles. Thus, the capability of sp-icpTOFMS to identify such particles is inequivalent.

Environmental and Societal Implications. This study has demonstrated that conventional waste-burning practices in arctic autochthonous communities release anthropogenic inorganic nanomaterials (metal oxides, chromates, and alloys) and nanoplastics in relatively significant quantities. The inorganic nanomaterials may have originated from the combustion of construction material (e.g., TiO2, CCA, and chromate pigments) and plastic additive waste (e.g., Sn, Sb, etc.), semiconductors (SnPb), and alloys (SbPb). These nanomaterials travel relatively long distances within the arctic autochthonous communities, spanning over 20 km, potentially exposing indigenous people to identified nanomaterials through air, water, and food. Other burning processes are common worldwide, such as burn pits, municipal waste burning practices, and wildland-urban interface fires, consume similar materials to those found in arctic autochthonous communities' waste and thus are likely to release similar types of anthropogenic nanomaterials into the surrounding environments, exposing much larger populations (millions of people) and other ecosystems to the same types of anthropogenic nanomaterials.

The identified anthropogenic nanomaterials are likely to be mobilized upon the melting of snow into waterways, potentially accumulating in sediments and marine organisms, such as mussels, clams, and other species higher up the food chain. These species are consumed by Arctic autochthonous communities, which poses a risk to their traditional food sources. Some of these identified nanomaterials are highly toxic, which could directly impact the health of Arctic autochthonous communities.

The presence of these toxic substances in Arctic autochthonous communities' environment and food resources can lead to significant health issues, threatening their wellbeing and traditional lifestyle.

The findings of this study highlight the importance of monitoring local anthropogenic nanomaterials within the arctic region, which has received much less attention compared with global contaminant sources. The results of this research empower local vulnerable Arctic autochthonous communities to advocate for solutions to minimize or eliminate exposure to locally emitted anthropogenic nanomaterials such as those emitted from open-air combustion in order. Potential solutions to minimize exposure to anthropogenic nanomaterials in the Arctic communities include promoting minimal packaging and reusable materials, launching community education campaigns to enhance awareness of waste minimization, and developing small-scale waste-to-energy plants.

This study highlights the necessity for a comprehensive, multielement, and multimolecular approach in the identification and tracking of anthropogenic nanomaterials in environmental samples. The identification and monitoring strategies developed in this study can be adapted and applied globally to track and mitigate anthropogenic nanomaterial.

### ASSOCIATED CONTENT

# Supporting Information

pubs.acs.org/est

The Supporting Information is available free of charge at https://pubs.acs.org/doi/10.1021/acs.est.4c02598.

Data obtained regarding particle size by AF4-SLS and electron microscopy data and all processed data obtained by sp ICPTOFMS (PDF)

#### AUTHOR INFORMATION

#### **Corresponding Authors**

Julien Gigault — Takuvik Laboratory, IRL3376 CNRS-Université Laval, G1 V 0A6 Quebec City, Quebec, Canada; orcid.org/0000-0002-2988-8942; Email: julien.gigault@takuvik.ulaval.ca

Mohammed Baalousha — South Carolina University, Environmental Health Sciences, Arnold School of Public Health, Columbia, South Carolina 29208, United States; orcid.org/0000-0001-7491-4954; Email: mbaalous@mailbox.sc.edu

## Authors

Caroline Guilmette — Takuvik Laboratory, IRL3376 CNRS-Université Laval, G1 V 0A6 Quebec City, Quebec, Canada Huiwen Cai — Takuvik Laboratory, IRL3376 CNRS-Université Laval, G1 V 0A6 Quebec City, Quebec, Canada; orcid.org/0000-0002-6468-7628

Charlotte Carrier-Belleau – Takuvik Laboratory, IRL3376 CNRS-Université Laval, G1 V 0A6 Quebec City, Quebec, Canada

Marie Le Bagousse – Takuvik Laboratory, IRL3376 CNRS-Université Laval, G1 V 0A6 Quebec City, Quebec, Canada; o orcid.org/0009-0005-5665-4374

Adèle Luthi-Maire — Takuvik Laboratory, IRL3376 CNRS-Université Laval, G1 V 0A6 Quebec City, Quebec, Canada Manon Gibaud — Takuvik Laboratory, IRL3376 CNRS-Université Laval, G1 V 0A6 Quebec City, Quebec, Canada

Armelle Decaulne – LETG Nantes, UMR65S4 CNRS-Université Nantes, Institut de géographie et d'aménagement de Nantes Université, 44312 Nantes, France

Mahbub Alam – South Carolina University, Environmental Health Sciences, Arnold School of Public Health, Columbia, South Carolina 29208, United States

Complete contact information is available at: https://pubs.acs.org/10.1021/acs.est.4c02598

#### Notes

The authors declare no competing financial interest.

#### ACKNOWLEDGMENTS

We acknowledge the financial support from the North Sentinel project of the Apogée program (Université Laval), the "International Emerging Action" program from the French CNRS, the Natural Sciences and Engineering Research Council of Canada (NSERC) through the Discovery program, the Centre for Northern Studies, and National Science Foundation (Grant 2101983 and 2345468). Additionally, we acknowledge the ARICE program, Henrik Carlsen from Denmark Police and Daniel Cron and Le Ponant for the logistic and scientific support, significantly facilitating our fieldwork (Site B). Lastly, we acknowledge the USCAN project under the OHMi Nunavik organization for providing the collected samples at Site A (Labex DRIIHM program "Investissements d'avenir" referenced ANR-11-LABX-0010).

#### REFERENCES

- (1) Zagozewski, R.; Judd-Henrey, I.; Nilson, S.; Bharadwaj, L. Perspectives on Past and Present Waste Disposal Practices: A Community-Based Participatory Research Project in Three Saskatchewan First Nations Communities. *Environ. Health Insights* **2011**, *5*, No. EHI.S6974.
- (2) Eisted, R.; Christensen, T. H. Environmental Assessment of Waste Management in Greenland: Current Practice and Potential Future Developments. *Waste Manag. Res.* **2013**, *31* (5), 502–509.
- (3) Wang, Z.; Chen, Z.; An, C. A Review on Solid Waste Management in Canadian First Nations Communities: Policy, Practices, and Challenges. *Clean. Waste Syst.* **2023**, *4*, No. 100074.
- (4) BAPE. L'état des lieux et la gestion des résidus ultimes, 2022. https://www.bape.gouv.qc.ca/fr/dossiers/etat-lieux-et-gestion-residus-ultimes/ (accessed 2023-09-04).
- (5) Eriksen, M.; Borgogno, F.; Villarrubia-Gómez, P.; Anderson, E.; Box, C.; Trenholm, N. Mitigation Strategies to Reverse the Rising Trend of Plastics in Polar Regions. *Environ. Int.* **2020**, *139*, No. 105704.
- (6) Tian, H.; Gao, J.; Lu, L.; Zhao, D.; Cheng, K.; Qiu, P. Temporal Trends and Spatial Variation Characteristics of Hazardous Air Pollutant Emission Inventory from Municipal Solid Waste Incineration in China. *Environ. Sci. Technol.* **2012**, 46 (18), 10364–10371.
- (7) Feng, X.; Melander, A. P.; Klaue, B. Contribution of Municipal Waste Incineration to Trace Metal Deposition on the Vicinity. *Water. Air. Soil Pollut.* **2000**, *119* (1), 295–316.
- (8) Li, C.; Yang, L.; Wu, J.; Yang, Y.; Li, Y.; Zhang, Q.; Sun, Y.; Li, D.; Shi, M.; Liu, G. Identification of Emerging Organic Pollutants from Solid Waste Incinerations by FT-ICR-MS and GC/Q-TOF-MS and Their Potential Toxicities. *J. Hazard. Mater.* **2022**, 428, No. 128220.
- (9) Liu, S.; Zhao, S.; Liang, Z.; Wang, F.; Sun, F.; Chen, D. Perfluoroalkyl Substances (PFASs) in Leachate, Fly Ash, and Bottom Ash from Waste Incineration Plants: Implications for the Environmental Release of PFAS. Sci. Total Environ. 2021, 795, No. 148468.
- (10) Davranche, M.; Lory, C.; Juge, C. L.; Blancho, F.; Dia, A.; Grassl, B.; El Hadri, H.; Pascal, P.-Y.; Gigault, J. Nanoplastics on the Coast Exposed to the North Atlantic Gyre: Evidence and Traceability. *NanoImpact* **2020**, *20*, No. 100262.
- (11) Wahl, A.; Le Juge, C.; Davranche, M.; El Hadri, H.; Grassl, B.; Reynaud, S.; Gigault, J. Nanoplastic Occurrence in a Soil Amended with Plastic Debris. *Chemosphere* **2021**, *262*, No. 127784.
- (12) Blancho, F.; Davranche, M.; Fumagalli, F.; Ceccone, G.; Gigault, J. A Reliable Procedure to Obtain Environmentally Relevant Nanoplastic Proxies. *Environ. Sci.-Nano* **2021**, 8 (11), 3211–3219.
- (13) Gigault, J.; El Hadri, H.; Reynaud, S.; Deniau, E.; Grassl, B. Asymmetrical Flow Field Flow Fractionation Methods to Characterize

- Submicron Particles: Application to Carbon-Based Aggregates and Nanoplastics. *Anal. Bioanal. Chem.* **2017**, 409 (29), 6761–6769.
- (14) Baalousha, M.; Wang, J.; Erfani, M.; Goharian, E. Elemental Fingerprints in Natural Nanomaterials Determined Using SP-ICP-TOF-MS and Clustering Analysis. *Sci. Total Environ.* **2021**, 792, No. 148426.
- (15) Wang, J.; Nabi, M. M.; Erfani, M.; Goharian, E.; Baalousha, M. Identification and Quantification of Anthropogenic Nanomaterials in Urban Rain and Runoff Using Single Particle-Inductively Coupled Plasma-Time of Flight-Mass Spectrometry. *Environ. Sci. Nano* **2022**, 9 (2), 714–729.
- (16) Lane, D. J.; Jokiniemi, J.; Heimonen, M.; Peräniemi, S.; Kinnunen, N. M.; Koponen, H.; Lähde, A.; Karhunen, T.; Nivajärvi, T.; Shurpali, N.; Sippula, O. Thermal Treatment of Municipal Solid Waste Incineration Fly Ash: Impact of Gas Atmosphere on the Volatility of Major, Minor, and Trace Elements. *Waste Manag.* **2020**, *114*, 1–16.
- (17) Raclavská, H.; Corsaro, A.; Hlavsová, A.; Juchelková, D.; Zajonc, O. The Effect of Moisture on the Release and Enrichment of Heavy Metals during Pyrolysis of Municipal Solid Waste. *Waste Manag. Res. J. Int. Solid Wastes Public Clean. Assoc. ISWA* **2015**, 33 (3), 267–274.
- (18) Gogos, A.; Wielinski, J.; Voegelin, A.; von der Kammer, F.; Kaegi, R. Quantification of Anthropogenic and Geogenic Ce in Sewage Sludge Based on Ce Oxidation State and Rare Earth Element Patterns. *Water Res. X* **2020**, *9*, No. 100059.
- (19) Gondikas, A.; von der Kammer, F.; Kaegi, R.; Borovinskaya, O.; Neubauer, E.; Navratilova, J.; Praetorius, A.; Cornelis, G.; Hofmann, T. Where Is the Nano? Analytical Approaches for the Detection and Quantification of TiO2 Engineered Nanoparticles in Surface Waters. *Environ. Sci. Nano* **2018**, 5 (2), 313–326.
- (20) Loosli, F.; Wang, J.; Rothenberg, S.; Bizimis, M.; Winkler, C.; Borovinskaya, O.; Flamigni, L.; Baalousha, M. Sewage Spills Are a Major Source of Titanium Dioxide Engineered (Nano)-Particle Release into the Environment. *Environ. Sci. Nano* **2019**, *6* (3), 763–777.
- (21) Nabi, M. M.; Wang, J.; Baalousha, M. Episodic Surges in Titanium Dioxide Engineered Particle Concentrations in Surface Waters Following Rainfall Events. *Chemosphere* **2021**, 263, No. 128261.
- (22) Nabi, M. M.; Wang, J.; Erfani, M.; Goharian, E.; Baalousha, M. Urban Runoff Drives Titanium Dioxide Engineered Particle Concentrations in Urban Watersheds: Field Measurements. *Environ. Sci. Nano* **2023**, *10* (3), 718–731.
- (23) Alshehri, T.; Wang, J.; Singerling, S. A.; Gigault, J.; Webster, J. P.; Matiasek, S. J.; Alpers, C. N.; Baalousha, M. Wildland-Urban Interface Fire Ashes as a Major Source of Incidental Nanomaterials. *J. Hazard. Mater.* **2023**, 443, No. 130311.
- (24) Alam, M.; Alshehri, T.; Wang, J.; Singerling, S. A.; Alpers, C. N.; Baalousha, M. Identification and Quantification of Cr, Cu, and As Incidental Nanomaterials Derived from CCA-Treated Wood in Wildland-Urban Interface Fire Ashes. *J. Hazard. Mater.* **2023**, 445, No. 130608.
- (25) Hahladakis, J. N.; Velis, C. A.; Weber, R.; Iacovidou, E.; Purnell, P. An Overview of Chemical Additives Present in Plastics: Migration, Release, Fate and Environmental Impact during Their Use, Disposal and Recycling. *J. Hazard. Mater.* **2018**, 344, 179–199.
- (26) Mehrabi, K.; Kaegi, R.; Günther, D.; Gundlach-Graham, A. Quantification and Clustering of Inorganic Nanoparticles in Wastewater Treatment Plants across Switzerland. *CHIMIA* **2021**, *75* (7–8), 642–642.
- (27) Jiménez, S.; Pérez, M.; Ballester, J. Vaporization of Trace Elements and Their Emission with Submicrometer Aerosols in Biomass Combustion. *Energy Fuels* **2008**, 22 (4), 2270–2277.
- (28) Gosselin, M.; Zagury, G. J. Metal(Loid)s Inhalation Bioaccessibility and Oxidative Potential of Particulate Matter from Chromated Copper Arsenate (CCA)-Contaminated Soils. *Chemosphere* **2020**, 238, No. 124557.

- (29) Turner, A.; Holmes, L. A. Adsorption of Trace Metals by Microplastic Pellets in Fresh Water. *Environ. Chem.* **2015**, *12* (5), 600–610.
- (30) Catrouillet, C.; Davranche, M.; Khatib, I.; Fauny, C.; Wahl, A.; Gigault, J. Metals in Microplastics: Determining Which Are Additive, Adsorbed, and Bioavailable. *Environ. Sci.-Process. Impacts* **2021**, 23 (4), 553–558.
- (31) Lithner, D.; Larsson, Å.; Dave, G. Environmental and Health Hazard Ranking and Assessment of Plastic Polymers Based on Chemical Composition. *Sci. Total Environ.* **2011**, 409 (18), 3309–3324
- (32) Devaraj, L.; S, J.; Balakrishnan, N.; Christopher Selvin, P Compound Semiconducting SnSb Alloy Anodes for Li Ion Batteries: Effect of Elemental Composition of Sn—Sb. Semicond. Sci. Technol. 2020, 35 (4), No. 045008.
- (33) Gao, Y.; Zou, C.; Yang, B.; Zhai, Q.; Liu, J.; Zhuravlev, E.; Schick, C. Nanoparticles of SnAgCu Lead-Free Solder Alloy with an Equivalent Melting Temperature of SnPb Solder Alloy. *J. Alloys Compd.* **2009**, 484 (1), 777–781.
- (34) Wu, C. M. L.; Yu, D. Q.; Law, C. M. T.; Wang, L. Properties of Lead-Free Solder Alloys with Rare Earth Element Additions. *Mater. Sci. Eng. R Rep.* **2004**, *44* (1), 1–44.
- (35) Liu, Y.; Yang, B.; Zhang, M.; Xia, B.; Chen, C.; Liu, X.; Zhong, J.; Xiao, Z.; Tang, J. Bournonite CuPbSbS3: An Electronically-3D, Defect-Tolerant, and Solution-Processable Semiconductor for Efficient Solar Cells. *Nano Energy* **2020**, *71*, No. 104574.
- (36) Liu, J.-J.; Lee, M.-W. Lead Antimony Sulfide Semiconductor-Sensitized Solar Cells. *Electrochim. Acta* **2014**, *119*, 59–63.
- (37) Song, J.; Peng, P. Characterisation of Black Carbon Materials by Pyrolysis—Gas Chromatography—Mass Spectrometry. *J. Anal. Appl. Pyrolysis* **2010**, *87* (1), 129–137.
- (38) Le Juge, C.; Grassl, B.; Allan, I. J.; Gigault, J. Identification of Polystyrene Nanoplastics from Natural Organic Matter in Complex Environmental Matrices by Pyrolysis—Gas Chromatography—Mass Spectrometry. *Anal. Bioanal. Chem.* **2023**, 415 (15), 2999—3006.
- (39) Blancho, F.; Davranche, M.; Hadri, H. E.; Grassl, B.; Gigault, J. Nanoplastics Identification in Complex Environmental Matrices: Strategies for Polystyrene and Polypropylene. *Environ. Sci. Technol.* **2021**, *55* (13), 8753–8759.
- (40) Watteau, F.; Dignac, M.-F.; Bouchard, A.; Revallier, A.; Houot, S. Microplastic Detection in Soil Amended With Municipal Solid Waste Composts as Revealed by Transmission Electronic Microscopy and Pyrolysis/GC/MS. Front. Sustain. Food Syst. 2018, 2, 81.
- (41) Xuan, W.; Yan, S.; Dong, Y. Exploration of Pyrolysis Behaviors of Waste Plastics (Polypropylene Plastic/Polyethylene Plastic/Polystyrene Plastic): Macro-Thermal Kinetics and Micro-Pyrolysis Mechanism. *Processes* **2023**, *11* (9), 2764.
- (42) Burkart, J.; Willis, M. D.; Bozem, H.; Thomas, J. L.; Law, K.; Hoor, P.; Aliabadi, A. A.; Köllner, F.; Schneider, J.; Herber, A.; Abbatt, J. P. D.; Leaitch, W. R. Summertime Observations of Elevated Levels of Ultrafine Particles in the High Arctic Marine Boundary Layer. *Atmospheric Chem. Phys.* **2017**, *17* (8), 5515–5535.
- (43) Kang, S.; Zhang, Y.; Qian, Y.; Wang, H. A Review of Black Carbon in Snow and Ice and Its Impact on the Cryosphere. *Earth-Sci. Rev.* 2020, 210, No. 103346.